Special Feature: Materials Analysis

Ion-conducting Analysis by Quasi-elastic Neutron Scattering

Hiroshi Nozaki and Kazuya Kamazawa

Report received on Sep. 19, 2011

■**ABSTRACT**‖ The ion conductive behaviors were studied by quasi-elastic neutron scattering (QENS) technique. The QENS spectra of superprotonic conductor; $CsHSO_4$ and $CsHSeO_4$ composed of one delta function and two Lorentzians. The two Lorentz components showed two different proton conducting diffusions. The QENS signals of lithium ions for lithium manganese spinels; $LiMn_2O_4$ and $Li_{1.1}Mn_{1.9}O_4$ were detected using the NIST as a neutron source and the both self diffusion coefficients were estimated as $\sim 10^{-8}$ cm^2 without affected by magnetic ions. This value was almost same as that obtained by μSR measurements.

■**KEYWORDS**‖ Quasi-elastic Neutron Scattering, Li Ion, Proton, Diffusion, Li-ion Secondary Battery, Fuel Cell

1. Introduction

Since ion diffusion is a basic principle behind the operation of batteries and fuel cells, it is very important to understand the mechanism of ion diffusion in solids in order to develop novel electrode and electrolyte materials. In particular, the current urgent issue is how to detect and control Li^+- and H^+-diffusion in solids, because both a Li-ion battery (LIB) and fuel cell (FC) are the key component for hybrid-vehicles (HV) and electronic-vehicles (EV). Besides electrochemical measurements, which provide a chemical diffusion coefficient (D^{chem}), there are mainly the following three techniques to detect a self-diffusion coefficient (D) in solids;

1) nuclear magnetic resonance (NMR),
2) muon-spin relaxation (μSR), and
3) quasielastic neutron scattering (QENS).

Among them, NMR is unambiguously the most common technique to measure D_{Li} and D_H,[1] since both Li and H are an NMR active nuclear. However, there arises difficulty to detect a diffusive behavior by NMR in the materials containing magnetic ions, because of the effect of electron spins on the spin-lattice relaxation rate. Also, it is difficult to analyze the multi components of diffusive motions because NMR detect only the average value of diffusion motions. We have, therefore, attempted to detect a diffusive behavior for $Li_{0.73}CoO_2$ by μSR[2-4] and found that Li ions start to diffuse above around 150 K. The estimated D_{Li} is larger by 4 or 5 orders of magnitude than that estimated by NMR, and is consistent with the prediction by first-principles calculations. However, since the jump rate of Li^+ becomes too fast for μSR above 300 K, we need another technique to detect Li diffusion, particularly at high temperatures. Here, we report our results of QENS studies on LIB and FC materials.

2. Quasi-elastic Neutron Scattering Experiment as a Probe for the Ionic Conducting Behavior

QENS is a powerful technique to detect a fast ionic motion in ionic-conducting materials, although IENS detects, in principle, phonons, for which a typical frequency ranges around 10^{13} Hz. However, IENS is insensitive to the motion below 1-10 μeV ($\sim 10^8$ –10^9 Hz). This means that QENS is a complementary technique to μSR.

The intensity of QENS is proportional to the incoherent scattering cross section (σ_{inc}) of the atom. Since the σ_{inc} of H is 80 barn (= 80 × 10^{-24} cm^2),[5] which is the largest value in all elements, the QENS signal from H is strong and easily detectable. Therefore, a lot of QENS studies have been performed for the materials containing H. On the other hand, the σ_{inc} of Li is 0.92 barn and is smaller by two orders of magnitude than σ_{inc} of H, resulting in a long measurement time to obtain a meaningful QENS signal from Li in old-generation neutron sources. Very

recently, an accelerator-based spallation neutron source was constructed both in Japan and the USA, i.e. J-PARC [6] and SNS.[7] Since they provide very intense neutron beams, we expect that QENS studies of Li will be more popular in the near future.

We have measured QENS spectra for super-protonic conductors and a cathode material of Li-ion batteries. The super-protonic conductors, $CsHSO_4$ (CHS) and $Rb_3H(SeO_4)_2$, are investigated as a candidate for the solid electrolyte of FC.[8] According to an initial QENS work on these materials by Belushkin et al. in 1987, there are two different proton motions in the super-protonic conductoring phase (Phase I) of CHS; that is, rotational motion and self-diffusion motion.[9] Using a jump diffusion model,[10] the diffusion length of the proton (λ_H) in Phase I was estimated as ~2.8 Å,[10] which corresponds to the distance to the second nearest neighboring (s.n.n) proton. D_H was also estimated as $\sim 1 \times 10^{-7}$ cm²/s at 423 K, and was consistent with the result of ^{1}H-NMR.[11] However, it is still difficult to explain the origin of super-protonic conductivity for CHS based only on these motions, because the estimated λ_H is too short to yield a conduction pathway along the whole lattice.

3. Superprotonic Conductors; CsHSO₄ and CsHSeO₄

CHS ($CsHSeO_4$ (CHSe)) exhibits two phase transitions at T_{III-II} = 330 K (323 K) and T_{II-I} = 414 K (401 K) (see **Fig. 1**). The three phases divided by T_{III-II} and T_{II-I} are called as Phase III, Phase II and Phase I from low-T to high-T. The proton conductivity σ_H for Phase I is $10^4 – 10^7$ times higher than that of Phase III. In order to understand the mechanism of the superprotonic conductive behavior, we performed QENS measurements for CHS and CHSe.
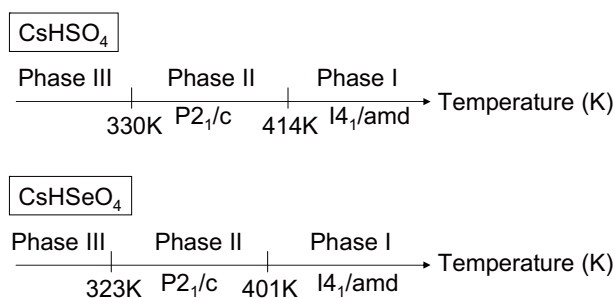

Fig. 1　Phase diagram of CsHSO₄ and CsHSeO₄.

3. 1 Sample Preparation and Experimental Method

Powder samples of $CsHSO_4$ (CHS) and $CsHSeO_4$ (CHSe) were prepared by crushing single crystals of CHS and CHSe. The details of the crystal growth were described in elsewhere.[12] The neutron measurements were carried out in the temperature (T) range between 250 and 463 K at high flux back scattering spectrometer (HFBS), the cold neutron back scattering spectrometer located at the NIST Center for Neutron Research in the U.S.A. Although the wave-length of incident neutron is 6.271 Å, the energy resolution is ~ 1 μeV due to a back scattering geometry.[13] To achieve dynamic range of ± 17 μeV, Si(111) crystal monochromator was operated at 24 Hz. Prior to experiment, both samples were kept in vacuum oven at room temperature to remove any signs of moisture.

3. 2 Experimental Results

Figure 2 shows the fixed window scan (FWS) data as a function of T for CHS and CHSe. The data was collected in the Doppler stopped mode of HFBS, where all the elastic neutrons were counted as a
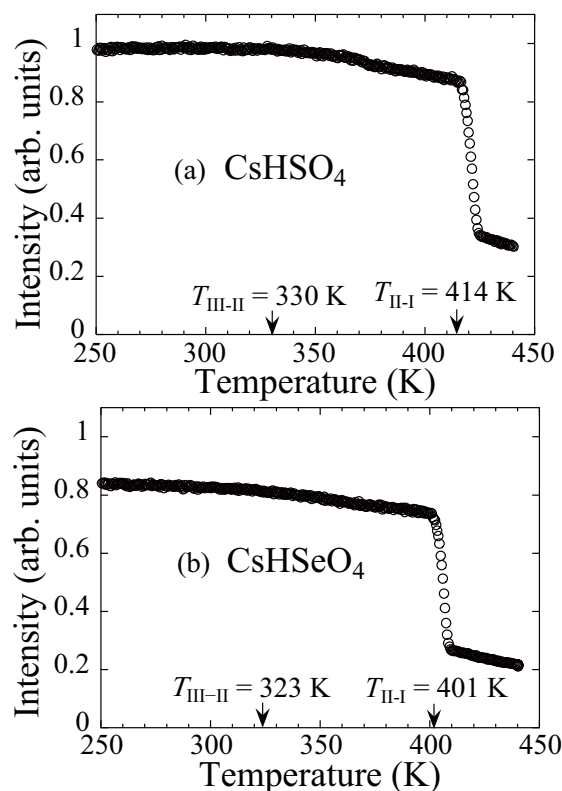

Fig. 2　Elastic intensity as function of temperature for (a) CsHSO₄ and (b) CsHSeO₄.

function of T. A drastic change be can seen clearly in the FWS-intensity at T_{II-I} for both CHS and CHSe. Interestingly, there is no change in intensity around T_{III-II}, although a small change is seen around 370 K for CHS. The change in the elastic intensity at T_{II-I} is estimated to be around ~70% for both samples. The large decrease in the elastic intensity is unambiguously attributed to the incoherent scattering of hydrogen, and not to the other ions, i.e. Cs, S and O as scattering cross sections of the later are very small. In other words, Fig. 2 indicates that the proton motion is static below T_{II-I}, whereas dynamic above T_{II-I} on backscattering time scales (~10 ns). Note that, as T increases from 250 K, the elastic intensity drops down to ~30% indicating hydrogen motion in nano-second time scale. The present setup (HFBS) is suitable for detecting such changes at T_{II-I}, due to its high energy-resolution. This also indicates that the dynamic proton motion directly correlates with super protonic conductivity (SPC), since SPC appears only above T_{II-I}.

Figure 3 shows energy spectra at 400 K and 463 K for CHS and at 390 K and 463 K for CHSe at $Q = 1.51$ Å^{-1}. Above this Q value, Bragg peaks at ($Q \sim 1.7$ Å^{-1})

interfere and data cannot analyzed. As we can see, the shape of the quasielastic spectra changes drastically across T_{II-I}. For Phase II, the shape and the width of the peak are the same as that of the resolution for CHS obtained at 4 K. This means that within the resolution of HFBS spectrometer (~ 1 µeV), the proton motion is static in Phase II, as expected from Fig. 1. On the other hand, for Phase I, the intensity at $E = 0$ decreases sharply and the peak width broadens due to the quasielastic scattering. The energy spectrum for Phase I was well fitted by two Lorentzians and one delta function. Instrument resolution was measured by measuring quasi-elastic spectra for CHS at 4 K where all intensity is elastic in nature.

The full width at half maximum $\Gamma_{FWHM}(Q)$ of the wide and narrow Lorentzian component is displayed as a function of Q and Q^2 in **Figs. 4**(a)-(d). The wide component (Figs. 4(a) and (c)) is thought to correspond to the self-diffusion of proton, which was already reported.[14] In fact, from our measurements diffusion lengths are estimated to be 3.7 Å (CHS) and 3.5 Å (CHSe) (solid lines), and are comparable to reported jump lengths of 2.8 Å (dashed lines) in Ref. (14). Here,
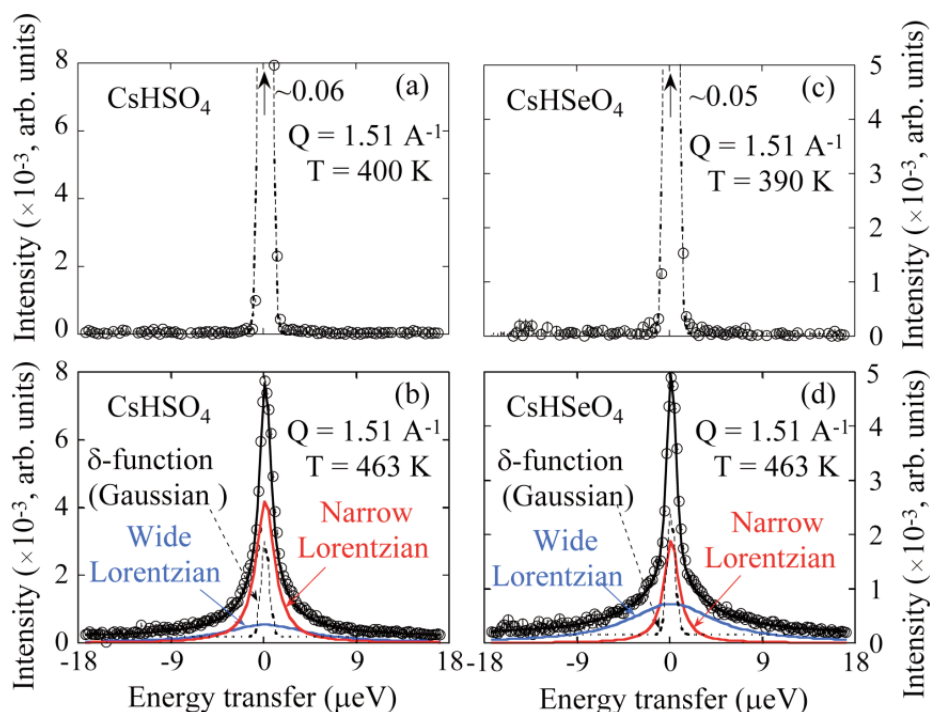

Fig. 3 The energy spectra at $Q = 1.51$ Å^{-1} at (a) 400 K, (b) 463 K for CsHSO$_4$ and at (c) 390 K and (d) 463 K for CsHSeO$_4$. In (b) and (d), one delta function and two Lorentzians are used to fit the spectra. The three components are also shown in (b) and (d) for clearly understanding the fit. The resolution function is obtained from the energy spectra of CsHSO$_4$ observed at 4 K. Throughout this paper, error bars represent standard deviation.

we have used the following fit function;

$$\Gamma_{\mathrm{FWHM}}(Q) = \left(\frac{1}{\tau}\right)\left[1 - \frac{\sin(Q\lambda_{\mathrm{H}})}{Q\lambda_{\mathrm{H}}}\right] \cdots \cdots (1)$$

where λ_{H} is diffusion length and τ is proton residence time. Using the relationship $D_{\mathrm{H}} = \lambda_{\mathrm{H}}^2/6\tau$,[10] $D_{\mathrm{H}}^{\mathrm{w}}$ for the wide component is estimated to be about 1.2 (CHS) and 1.3 (CHSe) $\times 10^{-7}$ cm²/s. On the other hand, the narrow component (Figs. 4(b) and (d)) should be assigned as the new proton motion, which is found in this work. The experimental fits provide λ_{H} = 5.9 (CHS) and 6.8 Å (CHSe) (solid lines), which corresponds to the s.n.n. SO_4 anion distance, or equivalently, to the seventh n.n. protons. As a result, $D_{\mathrm{H}}^{\mathrm{n}}$ for the narrow component is calculated as 3.9 (CHS) and 4.9 (CHSe) $\times 10^{-8}$ cm²/s. Although this is about a half of $D_{\mathrm{H}}^{\mathrm{w}}$ for the wide component, the presence of the narrow component yields the additional contribution to the total σ_{H}. Note that the energy of the rotational motion [14] is too high to be observed with this spectrometer. That is, the proton motion caused by the rotational motion (the order od $\omega \sim 10^{11}$ s^{-1}) is too fast to be visible on HFBS. Since the rotational motion

does not contribute to the QENS spectrum and the intensity of the QENS spectrum exhibits a drastic change at $T_{\mathrm{II-I}}$, the rotational motion is most unlikely to correlate with the SPC mechanism.

3. 3 Analysis for the Protonic Conduction

It is very interesting and surprising that λ_{H} = 5.9 (CHS) and 6.8 (CHSe) Å for Phase I. This may leads to the question whether the narrow component really exists. A narrow Lorentzian component exists beyond experimental uncertainties absolutely. This can be seen in Fig. 3(b) and (d) where narrow component of FWHM ~ 1 μeV is used to fit the data. In addition, if we use combination of one Lorentzian and one delta function, we cannot obtain reasonable fits, particularly for the tail of the scattering function. Another support for additional proton motion can be found in first principle calculations to explain SPC mechanism. The estimated λ_{H} (5.9 Å: CHS) and (6.8 Å: CHSe) is comparable to the prediction from the first principle calculations,[15] in which the proton diffusion to the s.n.n. SO_4 (~ 5.7 Å) is considered to explain the SPC mechanism. Here, the distance to the s.n.n. SO_4 corresponds to that to the fifth n.n. proton, indicating
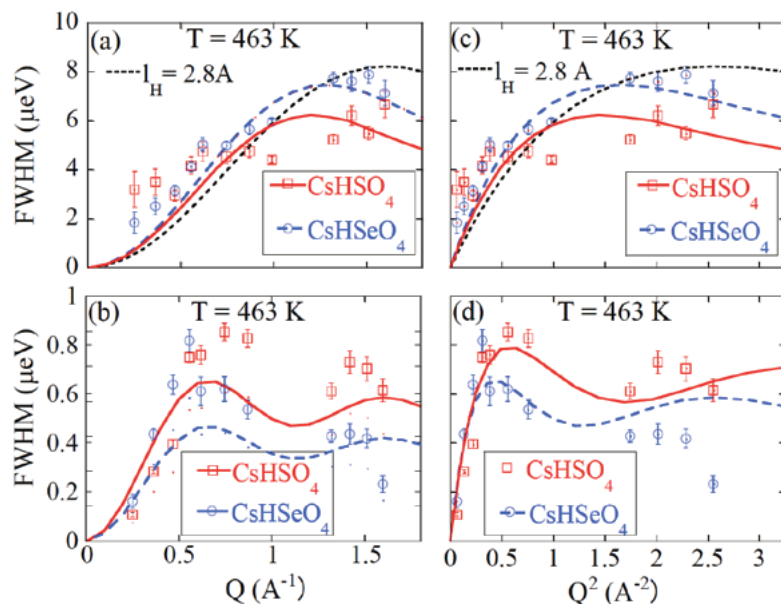

Fig. 4 The FWHM versus Q for (a) wide and (b) narrow component and the FWHM versus Q^2 for (c) wide and (d) narrow component for CsHSO₄ and CsHSeO₄. Solid and semi-dashed lines in (a) and (b) represent the fitting results jump diffusion model with λ_{H} = 3.7 Å and 3.5 Å. The fit function is $(1/\tau)((1-\sin(Q\lambda_{\mathrm{H}})/Q\lambda_{\mathrm{H}}))$, where λ_{H} is diffusion length and τ is proton residence time. The fits estimated λ_{H} = 3.7 and 3.5 Å for CsHSO₄ and CsHSeO₄, while λ_{H} = 2.8 Å in Ref. (9) is also plotted as dashed line in (a) and (c) for comparison.

an existence of possible long range diffusion. The proton diffusion length are shown with structure of Phase I of CHS in **Fig. 5**. The presence of the long range diffusion also makes a continuous conduction path throughout the whole proton site of the lattice. The Q dependences of the narrow component for CHS and CHSe are shown in Fig. 4(b) and (d). Interestingly, the $\Gamma_{FWHM}(Q)$ curves show a maxima around $Q \sim 0.6$ $Å^{-1}$, which give $\lambda_H = 5.9$ Å (CHS) and 6.8 Å (CHSe). Although nuclear Bragg peaks appear around $Q \sim 1.2$ $Å^{-1}$ and $Q = 1.7 \sim 1.75$ $Å^{-1}$ for CHS and CHSe, the effect of Bragg peaks on $\Gamma_{FWHM}(Q)$ around $Q \sim 0.6$ $Å^{-1}$ is expected to be very limited. Furthermore, multiple scattering[16] and neutron absorptions should not affect the $\Gamma_{FWHM}(Q)$ curve, because of the high transmission and cylindrical shape of the sample for the QENS measurements. The present result, therefore, reflects the intrinsic feature of CHS and CHSe. Although $D_H = 3.9$ (CHS) and 4.9×10^{-8} cm^2/s and $\lambda_H = 5.9$ Å (CHS) and 6.8 Å (CHSe), the new proton diffusion motion is most likely to be a predominant factor for SPC, because the diffusion path of this motion
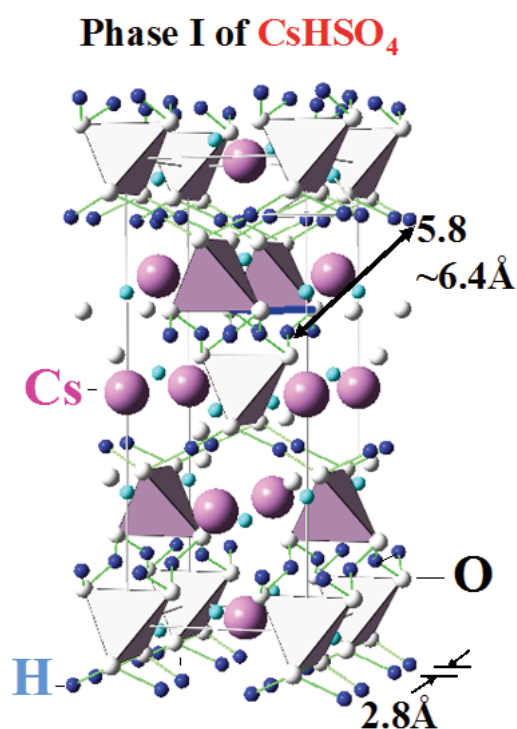

Fig. 5 The structure of CsHSO$_4$ and CsHSeO$_4$ of Phase I. Tetrahedra represent SO$_4$ or SeO$_4$ anions. The occupancy of the hydrogen site is 1/6.

overlaps so as to make a continuous conduction path.[17] Finally, in order to explain the origin of SPC, we should note the fact that there are 24 possible sites for 4 protons in Phase I, as in the case of the geometrical frustration in a Pauling's ice rule.[18,19]

4. Li Manganese Spinels as a Cathode Material for Li-ion Secondary Battery

4. 1 Sample Preparation and QENS Experiment

Powder samples of $^7LiMn_2O_4$ and $^7Li_{1.1}Mn_{1.9}O_4$ were prepared by a two-step solid state reaction from LiOH*H$_2$O and MnOOH. As previously reported,[20,21,22] highly crystallized LiMn$_2$O$_4$ compounds with $x < 0.15$ are available by this technique. Mixtures in proportional molar ratios of ^{7}LiOH*H$_2$O isotope (99.9% purity, Cambridge Isotope Laboratories, Inc., U. K.) and MnOOH (Tosoh Co. Japan) 99.9% purity, were ground and pressed into a pellet, and the pellet was heated at 1000°C for 12 hours in air. The fired pellet was crushed into powder, and the powder was re-pressed into a pellet, and then, the pellet was oxidized at 700°C for 24 hours in air for LiMn$_2$O$_4$, but 600°C for 24 hours in air for Li$_{1.1}$Mn$_{1.9}$O$_4$. In order to reduce the absorption of scattering neutron by ^{6}Li nuclei, the ^{7}Li-enriched chemical was used for the preparation. This gives us an advantage for using neutron scattering measurements, in particular with a long wavelength. Powder x-ray diffraction (XRD) studies indicated that the two samples were single phase of a cubic structure with a space group of $Fd\bar{3}m$. The magnetic susceptibility of the present samples were identical with the previous work.[20,23]

For the neutron experiment, two different spectrometers were used; one is Disk Chopper Spectrometer [24] (DCS) and the other is High Flux Back scattering Spectrometer [25] (HFBS). Both are installed at NCNR-NIST in the U.S.A. In the DCS measurements, we selected the neutron wavelength at 6.5 Å, while it was fixed at 6.27 Å for HFBS. The energy resolution of DCS is about 50 μeV, but that of HFBS is about 1 μeV due to the back scattering geometry. The T range for the measurements was 5-550 K on DCS and 80-500 K on HFBS. The powder samples were sealed in a vanadium-can with He-gas for DCS measurements and in an aluminum-can with air (ambient atmosphere) for HFBS measurements, respectively. The neutron data were packed, analyzed, and/or visualized using a computer program DAVE.[26]

4. 2 QENS Analyses

4. 2. 1 Neutron Scattering Data from Backscattering Spectrometer

Figure 6(a) shows the T dependence of the normalized mean-square displacement (MSD) $\delta\langle u^2\rangle =$
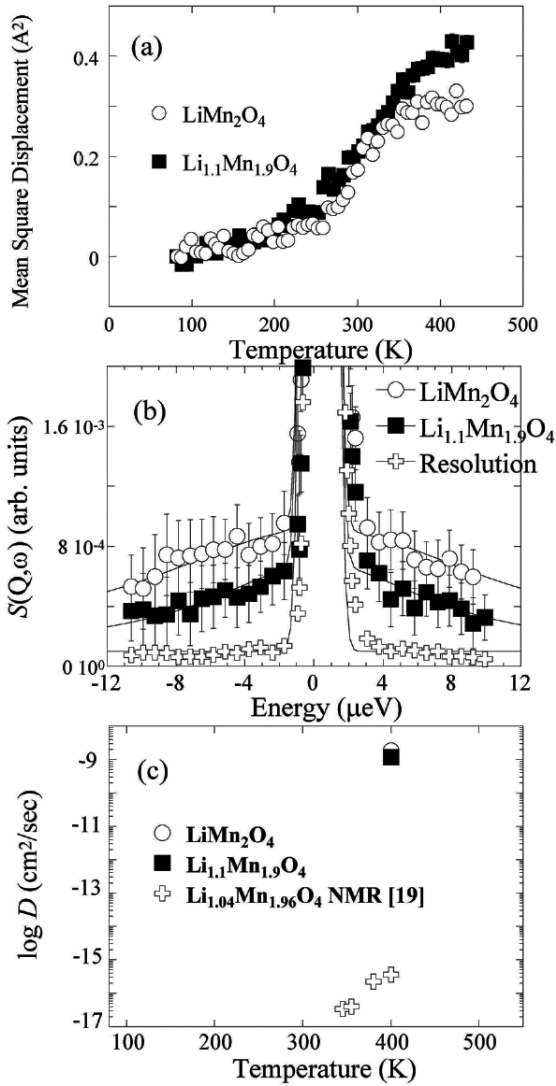

Fig. 6 (a) T dependence of the mean-square displacement for $LiMn_2O_4$ and $Li_{1.1}Mn_{1.9}O_4$. (b) The Q integrated energy spectra at 400 K of $LiMn_2O_4$ and $Li_{1.1}Mn_{1.9}O_4$. Full width at the half maximum is estimated to be 12.0(0) μeV and 7.7(1) μeV, respectively. To gain better statistics, the energy increment is rebinned from the original data. The spectrum comprises the data of the integrated intensities over the Q range between 0.25 and 1.75 Å^{-1}. (c) A comparison of diffusion coefficient of the present neutron and the previous NMR data of Ref. (29), in logarithmic scale.

$\langle u^2\rangle(T) - \langle u^2\rangle(T \rightarrow 0\text{K}),^{(26)}$ which is obtained from an elastic neutron scattering intensity of $^7LiMn_2O_4$ and $^7Li_{1.1}Mn_{1.9}O_4$. The measured intensity $I(Q, \omega)$ is given by a convolution of the incoherent scattering function $S_{inc}(Q, \omega)$ and resolution function $R(Q, \omega)$,

$$I(Q,\omega) = \int_{-\infty}^{\infty} S_{inc}(Q,\omega')R(Q,\omega-\omega')d\omega', \cdots (2)$$

$$\delta\langle u^2\rangle = \int_{-\infty}^{\infty} \mathcal{F}S_{inc}(Q,\omega=0)u^2 du, \cdots\cdots (3)$$

where $\mathcal{F}$ is the spatial Fourier transform operator, Q is the momentum transfer, ω is the energy transfer, and u is the displacement. For the both samples, as T increases from 90 K, $\delta\langle u^2\rangle$ increases up to ~ 360 K, but the slope $(d\delta\langle u^2\rangle/dT)$ suddenly increases at around 280 K. Above 360 K, $\delta\langle u^2\rangle$ for $^7Li_{1.1}Mn_{1.9}O_4$ levels off to a constant value up to 460 K, while $\delta\langle u^2\rangle$ for $^7LiMn_2O_4$ slowly increases up to 460 K. The anomaly at ~ 280 K indicates that the lattice vibration deviates from the Debye's approximation above 280 K. The anomaly is naturally caused by the diffusion of the ions with a incoherent neutron scattering cross section (σ_{inc}) (i.e., Li and/or Mn ion). On the other hand, since σ_{inc} of oxygen is negligibly small (0.0008 barn) compared with those for Mn (0.4 barn) and ^7Li (0.78 barn),[10] neither the shift of oxygen position nor oxygen deficiency contributes to the change in the slope at ~280 K. This means that Li ions start to diffuse above 280 K, because if the Mn ions diffuse at $T \geq 280$ K, the spinel framework could not be stable at room T. Similar diffusive behavior was also reported by μ$^+$SR measurements.[27]

Figure 6(b) shows the energy spectra for both $^7LiMn_2O_4$ and $^7Li_{1.1}Mn_{1.9}O_4$ at 400 K. A QENS signal is clearly observed together with an elastic signal that defines an instrumental resolution. The spectra are, thus, fitted by a combination of a delta function $\delta(\omega)$, which comes from the instrumental resolution, and a Lorentz function.

$$I(Q_0,\omega) = \int_{-\infty}^{\infty} S_{inc}(Q_0,\omega')R(Q_0,\omega-\omega')d\omega',$$
$$\cdots\cdots\cdots\cdots (4)$$

$$S_{inc}(Q_0,\omega') = A(Q_0)\delta(\omega') + \frac{1}{\pi}\frac{\Gamma_{Q_0}}{\Gamma_{Q_0}^2 + \hbar^2(\omega'-\omega_0)^2},$$
$$\cdots\cdots\cdots\cdots (5)$$

in which $A(Q_0)$ is the intensity of the δ function, Γ_{Q_0} is the width of the Lorentzian, and $\hbar$ is the Planck's constant. The Lorentzian fit provides a full width at half maximum (FWHM, Γ_{Q_0}) for ^{7}LiMn$_2$O$_4$ ~ 12.0(0) μeV, and for ^{7}Li$_{1.1}$Mn$_{1.9}$O$_4$ ~ 7.7(1) μeV. Note that FWHM of the QENS from the magnetic diffuse scattering ranges in meV order at low T and is out of the measurable range for HFBS. Therefore, there are no magnetic contributions to the estimated Γ_{Q_0}. Using the equation $\Gamma_{Q_0} = D_s^{Li}Q^2$, we obtain $D_s^{Li} = 1.8(4) \times 10^{-8}$ cm^2/s at 400 K for ^{7}LiMn$_2$O$_4$, and $1.1(8) \times 10^{-8}$ cm^2/s at 400 K for ^{7}Li$_{1.1}$Mn$_{1.9}$O$_4$, when we assume that $Q_0 \sim 1$ Å^{-1}. This is an averaged Q value for the spectrometer and is a typical value for the ionic diffusion length in solids.[28]

Surprisingly, the obtained D_s^{Li} is larger by six orders of magnitude than D_s^{Li} for LiMn$_2$O$_4$ estimated by Li-NMR[1] (see Fig. 6(c)). However, it is well known that the spin-lattice relaxation rate of the NMR signal is strongly affected by magnetic ions, resulting in difficulty in estimating correct D_s^{Li}.[2] Although there are, to our knowledge, no reports on the reliable D_s^{Li} for LiMn$_2$O$_4$, first principle calculations of D_s^{Li} for the other spinel, LiTi$_2$O$_4$, predicted that ranges around 2×10^{-10} cm^2/s at 300 K.[29] Furthermore, recent μ^+SR measurements on LiCoO$_2$ provided that for Li$_{0.73}$CoO$_2$ ranges around 7×10^{-10} cm^2/s at 300 K.[30] Therefore,

the obtained D_s^{Li} for LiMn$_2$O$_4$ by QENS is reasonable for the electrode material of Li ion batteries.

In order to know reliability or reproducibility of the $\delta\langle u^2\rangle(T)$ curve, $\delta\langle u^2\rangle$ for the two samples were measured several times (see **Figs. 7**(a) and (b)). The $\delta\langle u^2\rangle(T)$ curve obtained on the first heating run ($\delta\langle u^2\rangle_{1st}(T)$) exhibits a clear change in the slope at 280 K for both samples, as already explained (see Fig. 6(a)). However, the $\delta\langle u^2\rangle(T)$ curve obtained on the second heating run ($\delta\langle u^2\rangle_{2nd}(T)$) deviates from the $\delta\langle u^2\rangle_{1st}(T)$ curve, particularly above 280 K, that is, $\delta\langle u^2\rangle_{2nd}$ increases monotonically with T until 480 K. When the samples were heated above 280 K, such behavior was always observed regardless of both the heating and cooling rate.

Interestingly, the $\delta\langle u^2\rangle(T)$ curve obtained two days later ($\delta\langle u^2\rangle_{afd}(T)$) is found to be the same as the $\delta\langle u^2\rangle_{1st}(T)$ curve. Furthermore, the $\delta\langle u^2\rangle_{2nd}(T)$ curve obtained immediately after the $\delta\langle u^2\rangle_{afd}$ run deviates from the $\delta\langle u^2\rangle_{afd}(T)$ curve again. Therefore, this phenomenon is reproducible with thermal history. Such a slow phenomenon was never reported so far from other physical property measurements, such as structural, magnetic, and electric transport measurements. According to Ref. (31), oxygen deficiencies are formed above 973 K under ambient atmosphere. Therefore, the abnormal behavior of the
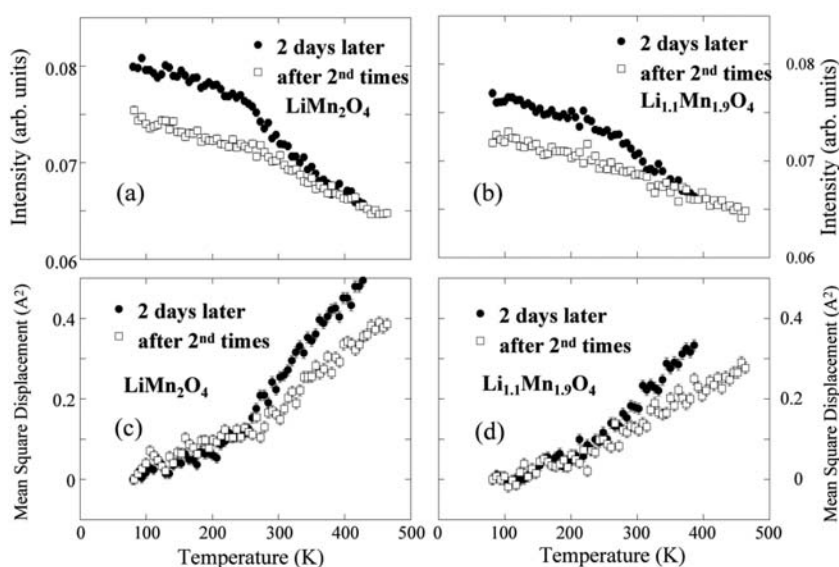
Fig. 7 T dependence of the elastic intensity (the mean-square displacement) for (a) [(c)] LiMn$_2$O$_4$ and (b) [(d)] Li$_{1.1}$Mn$_{1.9}$O$_4$. Solid circles show the data obtained in the second heating run after 2-day interval. Such interval makes the data the same as those obtained in the initial heating run. Open squares show the data obtained in the third heating run immediately after the second heating run. The error bar for each data point is smaller than the size of the symbols.

$\delta\langle u^2\rangle(T)$ curve with thermal history is not attributed to the oxygen deficiencies during the measurements below 500 K, since the sample was sealed in an aluminum can under ambient atmosphere. The behavior is, hence, connected with the diffusion of Li^+ at high T, particularly above 280 K. Such a thermal history and a slow recovery process imply that the Li^+ ions enter into a liquid-like state above 280 K. On the contrary, the Li^+ ions form a stable spinel lattice below 280 K. In other words, they are no longer a component of the rigid lattice above 280 K, while they return to a solid state below 280 K. More correctly, such a solid state is unlikely an usual crystalline solid but most likely an amorphous-like (or glass-like) solid, as in the case for a quenched glass from a high-T liquid phase. Since the amorphous-like state is a quasistatic state, the Li^+ ions are expected to move back to a regular Li site in the spinel lattice for several days.

Finally, it should be noted that the overall diffusive behavior of the Li^+ ions in $^7LiMn_2O_4$ is very similar to that in $^7Li_{1.1}Mn_{1.9}O_4$, despite the absence of a structural phase transition for $Li_{1.1}Mn_{1.9}O_4$. This naturally leads to the question why the Li^+ ion starts to diffuse at 280 K for both compounds. In order to respond to this question, we have studied the magnetic and structural nature of both compounds in detail by elastic and inelastic neutron scattering.

4. 2. 2 Neutron Scattering Data from Disk-chopper Time-of-flight Spectrometer

Figure 8 shows color contour maps of the neutron scattering intensity $I(Q, \omega)$ as a function of both wave vector Q and energy transfer $E (= \hbar\omega)$. In order to
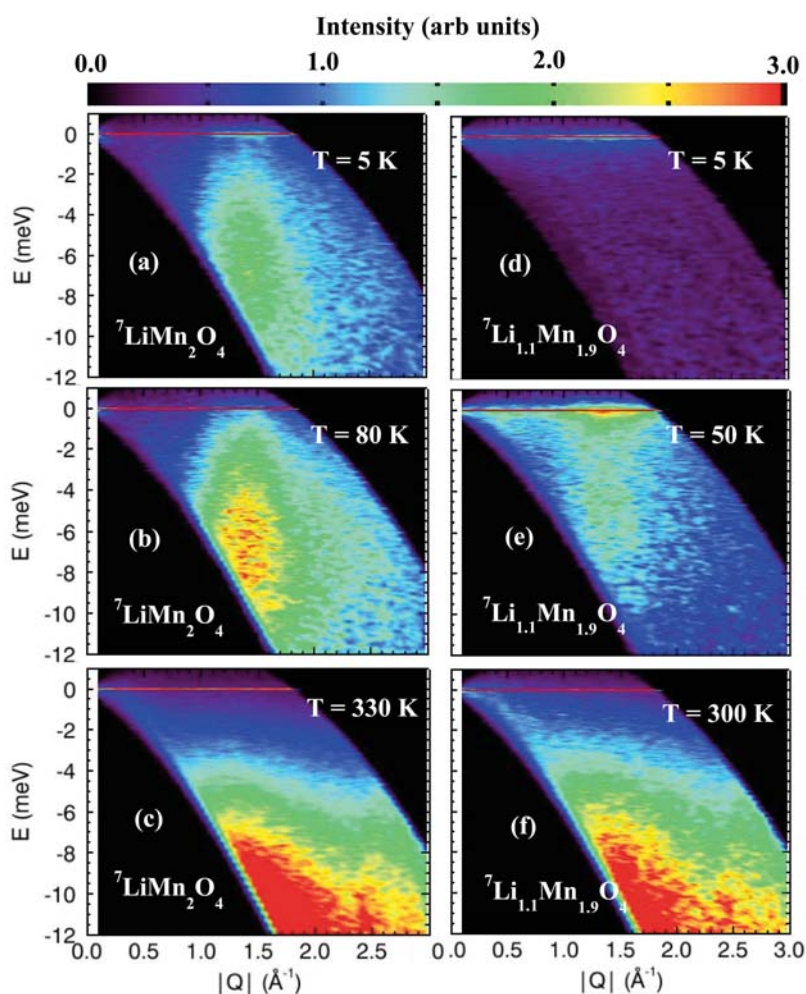

Fig. 8   Neutron scattering intensity as a function of energy transfer (E) and wave vector (Q) obtained at (a) 5 K, (b) 80 K, and (c) 330 K for $LiMn_2O_4$, (d) 5 K, (e) 50 K, and (f) 300 K for $Li_{1.1}Mn_{1.9}O_4$.

emphasize the change with T and the Li content, the maps are not corrected by the K_i/K_f factor, where K_i is the incident wave vector and K_f is the final wave vector. For $^7LiMn_2O_4$, magnetic excitations measured at the lowest T (= 5 K) are clearly observed in the low E region since its T_N is ~65 K. The magnetic excitations are, however, still visible even at 80 K. Note that there are no clear changes between the map obtained at 5 K and that at 80 K. At 330 K, the dominant signal comes from thermal fluctuation, because of the Q-independent I (Q, ω). For $^7Li_{1.1}Mn_{1.9}O_4$, on the other hand, there are no visible excitations measured at 5 K in the whole Q and E region (compare Fig. 8(d) with Fig. 8(a)). At 50 K, which is above T_f (~25 K), either quasi- or inelastic

excitation is visible, indicating that the frozen magnetic moments become dynamic. At 300 K, the map is eventually the same as that of $^7LiMn_2O_4$ at 330 K (Fig. 8(c)). These maps clarify the overall differences of magnetic excitations between $^7LiMn_2O_4$ and $^7Li_{1.1}Mn_{1.9}O_4$.

Figure 9 shows the elastic and the inelastic neutron scattering profiles as a function of Q for $LiMn_2O_4$. All the data were, hereafter, corrected by the K_i/K_f factor. At 5 K (Fig. 9(a)), which is well below T_N (= 65 K), many magnetic Bragg peaks are observed in the elastic profile. Since each magnetic Bragg peak appears at the incommensurate position to the lattice period, it is difficult to determine the spin structure, based only on the present data obtained in the Q range below 1.8 Å^{-1}.

Fig. 9　Elastic and inelastic neutron scattering profiles as a function of wave vector Q for $LiMn_2O_4$. The displayed Ts were (a) and (d) 5 K, (b) and (e) 80 K, (c) and (f) 330 K. Here, to split the elastic and inelastic contribution, the elastic and the inelastic scattering intensity is integrated in the range -0.02 meV $< E < 0.02$ meV and -2 meV $< E < -0.1$ meV, respectively. Due to an allowed kinematic region of the spectrometer of E versus Q, the minus E side was used in the inelastic scattering data. Numbers on the top of (a) represent the intensity of each magnetic peak. Minus values in the horizontal axis of the inset of (d) and (e) mean the energy gain from the incident neutron. The dashed line in (a) indicates the shape of the inelastic neutron scattering pattern of (d). The three peaks observed at Q ~1.6, 1.65, and 1.7 Å^{-1} in the elastic profile (a), (b), and (c) are caused by contaminations from the cryostat or the other components (e.g., the sample holder, because we did not use a Cd mask due to its low melting point).

It is also found that a broad peak coexists with the magnetic Bragg peaks in the Q range above 0.8 Å^{-1}. The origin of the broad peak is most unlikely a magnetic diffuse scattering, because the shape of the broad peak corresponds to that of the magnon peak in the inelastic neutron scattering profile (Fig. 9(d)). At 80 K (Fig. 9(b)), there are no magnetic peaks but nuclear Bragg peaks in the elastic scattering profile. More correctly, there are two types of nuclear Bragg peaks; one is assigned as superlattice reflections and is observable only below $T_t = 280$ K. The other is the 111 nuclear reflection at $Q = 1.32$ Å^{-1}, which is seen even at 330 K (Fig. 9(c)). The presence of the superlattice reflections is the evidence that the CO-CDO transition occurs at 280 K. Here, we should note that the Li$^+$ ions start to diffuse above 280 K. This is quite reasonable in order to keep local charge neutrality during the Li$^+$ diffusion.

In the inelastic scattering profile, a magnetic broad peak exists not only at 5 K (Fig. 9(d)) but also at 80 K (Fig. 9(e)) (i.e., well above T_N(= 60 K)). The FWHM of the QENS at 5 K and 80 K (see the inset of Figs. 9(d) and (e)) is roughly estimated as a few meV, which is very different from the energy for the Li$^+$ diffusion, as described in Sec. 4. 2. 1. In addition, since the intensity of the magnetic broad peak at 80 K is larger than that at 5 K, long-range magnetic correlation is static at low T but dynamic at high T. Interestingly, the shape of the magnetic broad peak at 80 K looks very similar to that at 5 K, and finally, the inelastic broad peak disappears completely at 330 K (Fig. 9(f)). This indicates that, even above T_N, the arrangement of the Mn spins (Mn^{3+} and Mn^{4+}) is basically the same as that for the low T ($< T_N$) phase. However, the spin correlation is already dynamic at 80 K.

In contrast to ^{7}LiMn$_2$O$_4$, the elastic scattering profile at 5 K for ^{7}Li$_{1.1}$Mn$_{1.9}$O$_4$ consists of a magnetic diffuse scattering and the 111 nuclear Bragg peak (see **Fig. 10**(a)). There is neither magnetic Bragg peak nor superlattice reflection. Only the 111 nuclear Bragg peak is observed in the elastic profile at 50 K (Fig. 10(b)). The data obtained at $T \geq 50$ K (e.g., $T =$

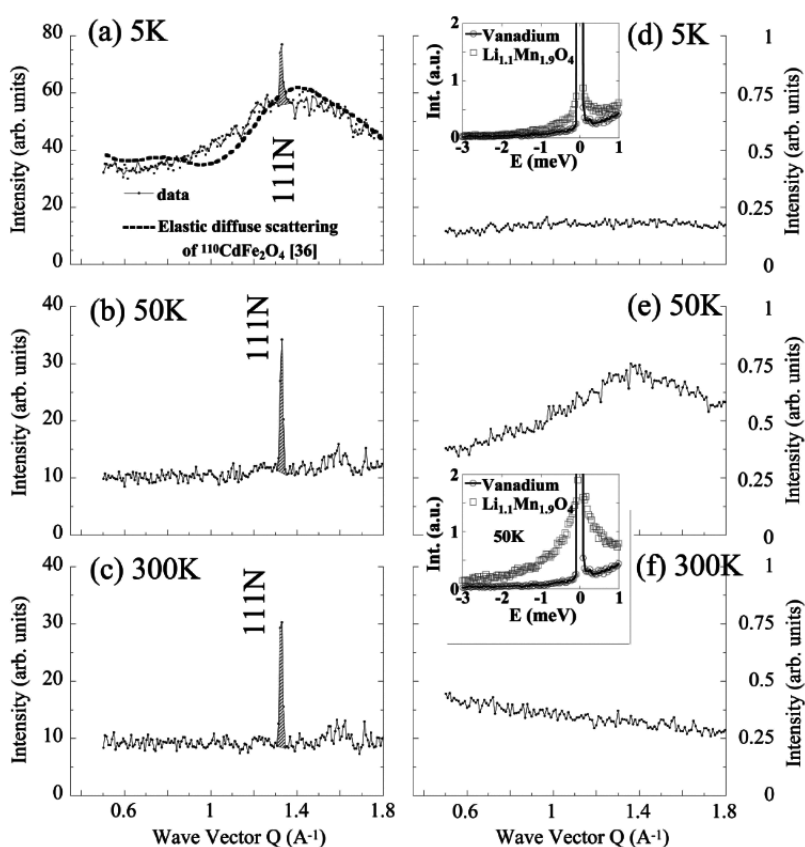**Fig. 10** Elastic and inelastic neutron scattering profiles as a function of wave vector Q for Li$_{1.1}$Mn$_{1.9}$O$_4$. The displays were (a) and (d) 5 K, (b) and (e) 80 K, (c) and (f) 330 K. The dashed line in (a) indicates the diffraction data of ^{110}CdFe$_2$O$_4$ powder.[31]

300 K) (Fig. 10(c)), is essentially the same as that of 50 K, indicating the cubic symmetry for $^7Li_{1.1}Mn_{1.9}O_4$ in the whole measured T range.

Interestingly, in the inelastic scattering profile, there is no dynamic component at 5 K. This implies that all magnetic components freeze at low T. Although it is difficult to explain this unusual behavior at present, some magnetic excitations would exist in a higher energy region to satisfy the energy conservation law. At 50 K, a broad peak appears around $Q = 1.4$ Å^{-1} in the inelastic profile (Fig. 10(e)). This means that all magnetic components are static at 5 K, but they are dynamic at 50 K. The energy spectra are also shown in the inset of Figs. 10(d) and (e). Again the FWHM of the QENS spectra at 5 K and 80 K are in meV energy range, which is far above the detectable range of HFBS. Therefore, such FWHM does not affect the QENS spectra caused by the Li$^+$ diffusion observed in a µeV energy range.

The shape of the magnetic broad peak at 50 K is very different from that for $^7LiMn_2O_4$ at 80 K (Fig. 9(e)), suggesting a different spin configuration of the Mn ions between $^7LiMn_2O_4$ and $^7Li_{1.1}Mn_{1.9}O_4$. However, we should note that the shape of the magnetic broad peak at 50 K is very similar to that of the magnetic diffuse scattering at 5 K (Fig. 10(a)). Therefore, the spin configuration at 50 K is expected to resemble that at 5 K.

5. Conclusion

We have performed the QENS measurements for super-protonic conductors and Li manganese spinels to investigate the ionic conducting behavior. For the super-protonic conductors, we have found two different protonic diffusion motions corresponding to the super-protonic conducting behavior. For Li manganese spinels, we have succeeded in distinguishing between the signals from Li$^+$ motions and magnetic excitation of Mn moments because the energy scale of the magnetic excitation are different from the QENS energy range. Consequently, we have found that the diffusive behavior of Li$^+$ above 280 K for both $LiMn_2O_4$ and $Li_{1.1}Mn_{1.9}O_4$ and a self-diffusion coefficient was estimated as $\sim 10^{-8}$ cm^2/s at 400 K for both compounds. The QENS signals for the hydrogen compounds are easily detectable due to the high neutron incoherent cross section (σ_{inc}) of hydrogen. On the other hand, the σ_{inc} of lithium is two orders of magnitude smaller than that of hydrogen. Therefore,

it was difficult to perform QENS measurements for lithium compounds. However, due to the high neutron flux facilities such as J-PARC and SNS, the QENS measurement of lithium have become possible. Since we have succeeded in detecting the Li diffusive behavior by the QENS, it should be applied to the various ion conducting material composed by other ion such as Na, K and I.

References

(1) Verhoeven, V. W. J., de Schepper, I. M., Nachtegaal, G., et al., *Phys. Rev. Lett.*, Vol.86 (2001), pp.4314-4317.
(2) Sugiyama, J., Mukai, K., Ikedo, Y., et al., *Phys. Rev. Lett.*, Vol.103 (2009), 147601.
(3) Sugiyama, J., Ikedo, Y., Mukai, K., et al., *Phys. Rev. B*, Vol.82 (2010), 224412.
(4) Sugiyama, J., Nozaki, H., Harada, M., et al., *Phys. Rev. B*, Vol.84 (2011), 054430.
(5) Searsa, V. F., *Neutron News*, Vol.3 (1992), pp.29-37.
(6) *J-PARC* (*Japan Proton Accelerator Research Complex*), <http://j-parc.jp/index.html>.
(7) *ORNL Neutron Sciences*, <http://neutrons.ornl.gov/>.
(8) Haile, S. M., Boysen, D. A., Chisholm, C. R. I. and Merle, R. B., *Nature*, Vol.410 (2001), pp.910-913.
(9) Belushkin, A. V., Carlile, C. J. and Shuvalov, L. A., *J. Phys. Cond. Mat.*, Vol.4 (1992), pp.389-398.
(10) Chudley, C. T. and Elliot, R. J., *Proc. Phys. Soc.*, Vol.77 (1961), pp.353-361.
(11) Blinc, R., *Phys. Status Solidi b*, Vol.123 (1984), pp.K83-K87.
(12) Yoshida, Y., Matsuo, Y. and Ikehata, S., *J. Phys. Soc. Jpn.*, Vol.72 (2003), pp.1590-1591.
(13) Meyer, A., Dimeo, R. M., Gehring, P. M. and Neumann, D. A., *Rev. Sci. Instrum.*, Vol.74 (2003), pp.2759-2777.
(14) Belushkin, A. V., Carlile, C. J. and Shuvalov, L. A., *J. Phys. Cond. Mat.*, Vol.4 (1992), pp.389-398.
(15) Ke, X. and Tanaka, I., *Phys. Rev. B*, Vol.69 (2004), 165114.
(16) Zorn, R., *Nucl. Instrum. Methods Phys. Res.* Sect. A, Vol.572 (2007), pp.874-881.
(17) Belushkin, A. V., McGreevy, R. L., Zetterstrom, P. and Shuvalov, L. A., *Physica B*, Vol.241-242 (1998), pp.323-325.
(18) Pauling, L., *J. Am. Chem. Soc.*, Vol.57 (1935), pp.2680-2684.
(19) Chisholm, C. R. I. and Haile, S. M., *Chem. Mater.*, Vol.19 (2007), pp.270-279.
(20) Sugiyama, J., Mukai, K., Ikedo, Y., et al., *Phys. Rev. B*, Vol.75 (2007), 174424.
(21) Kitagawa, M., Wakabayashi, H., Ariyoshi, K. and Ohzuku, T., *ITE Lett. on Batteries, New Technol. & Medicine*, Vol.8 (2007), p.119.
(22) Mukai, K., Sugiyama, J., Ikedo, Y., Nozaki, H., et al.,

J. Phys. Chem. C, Vol.114 (2010), pp.11320-11327.

(23) Sugiyama, J., Mukai, K., Ikedo, Y., et al., *J. Mater. Sci.: Mater. Electron.*, Vol.19 (2008), pp.875-882.

(24) Copley, J. R. D. and Cook, J. C., *Chem. Phys.*, Vol.292 (2003), pp.477-485.

(25) Meyer, A., Dimeo, R. M., Gehring, P. M. and Neumann, D. A., *Rev. Sci. Instrum.*, Vol.74 (2003), pp.2759-2777.

(26) Azuah, R. T., Kneller, L. R., Qiu, Y., et al., *J. Res. Natl. Inst. Stand. Technol.*, Vol.114 (2009), pp.341-358.

(27) Kaiser, C. T., Verhoeven, V. W. J., Gubbens, P. C. M., et al., *Phys. Rev. B*, Vol.62 (2000), pp.R9236-R9239.

(28) Hempelmann, R., *Quasielastic Neutron Scattering and Solid State Diffusion* (2000), Clarendon Press Oxford, New York.

(29) Bhattacharya, J. and Van der Ven, A., *Phys. Rev. B*, Vol.81 (2010), 104304.

(30) Sugiyama, J., Atsumi, T., Hioki, T., et al., *J. Alloys Compd.*, Vol.235 (1996), pp.163-169.

(31) Kamazawa, K., Hashiguchi, S. and Tsunoda, Y., *JAERI-Review*, (2003), p.105.

Hiroshi Nozaki
　Research Field:
　　- Crystal Structure Analysis and Ion-conduction Analysis Using X-ray, Neutron and μSR
　Academic Degree: Dr. Eng.
　Academic Societies:
　　- The Physical Society of Japan
　　- The Japan Institute of Metals
　　- The Japanese Society for Synchrotron Radiation Research
　　- The Japanese Society for Neutron Science
　　- Society of Muon and Meason Science of Japan

Kazuya Kamazawa*
　Research Field:
　　- Neutron Scattering Experiments
　Academic Degree: Dr. Sci.
　Academic Societies:
　　- The Physical Society of Japan
　　- The Japan Institute of Metals
　　- The Japanese Society for Neutron Science
　Present Affiliation:
　　Comprehensive Research Organization for Science and Society

*Retired from TCRDL